EEET ECOLOGICAL ENGINEERING & ENVIRONMENTAL TECHNOLOGY

Ecological Engineering & Environmental Technology, 2025, 26(4), 311–322
https://doi.org/10.12912/27197050/200918
ISSN 2719–7050, License CC-BY 4.0

Received: 2025.01.04
Accepted: 2025.02.21
Published: 2025.03.01

Estimating land and sea surface temperatures using remote sensing and GIS: Insights into built-up areas and lithological formations in Aqaba, Jordan

Majed Ibrahim[1*], Ahmad AlShdaifat[2], Emad Al-Rjoub[1], Tamer El-Sayed Ali[3], Haya Al Taweel[4]

[1] Department of Geographic Information System and Remote Sensing, Faculty of Earth and Environmental Sciences, Al al-Bayt University, Mafraq, Jordan
[2] Department of Applied Erath and Environmental Sciences, Faculty of Earth and Environmental Sciences, Al al-Bayt University, Mafraq, Jordan
[3] Oceanography Department, Faculty of Science, Alexandria University, Alexandria, Egypt
[4] Royal Scientific Society, Amman, Jordan
* Corresponding author's e-mail: majed.ibrahim@aabu.edu.jo

ABSTRACT

This study aims to estimate land and sea surface temperatures (LST and SST) in Aqaba, Jordan, using remote sensing and GIS techniques and to explore their relationships with urban development and lithological formations. Landsat 8 OLI/TIRS and MODIS data were utilized, with LST estimated using the split-window algorithm and SST derived from MODIS. Land use and lithological maps were integrated to analyze temperature variations. The results revealed a moderate correlation ($R^2 = 0.64$) between MODIS and Landsat LST data. Maximum temperatures reached 47.76°C in urban areas and 50.45°C in exposed geological formations. The study highlights the significant impact of land use and lithology on surface temperatures, providing insights for urban planning and environmental management in coastal regions. Uncertainties due to atmospheric conditions and spatial resolution were noted. The findings offer practical value for climate resilience strategies and sustainable urban development. This research fills a gap in understanding the thermal dynamics of rapidly urbanizing coastal areas, particularly in arid regions like Aqaba.

Keywords: land surface temperature, sea surface temperature, GIS, remote sensing, lithological formations.

INTRODUCTION

Climate change remains one of the most pressing global challenges, with significant implications for environmental, social, and economic systems (Merigan and Weiss, 1980; Santer et al., 1996; Stanhill and Cohen, 2001; Vale et al., 2021; Wigley and Raper, 1990).Among its many impacts, rising land surface temperatures (LST) and sea surface temperatures (SST) have emerged as critical indicators of environmental change, particularly in rapidly urbanizing regions (Houghton and Woodwell, 1989; Warrick et al., 1996). While extensive research has been conducted on LST and SST in temperate and tropical regions, arid coastal cities, such as Aqaba, Jordan, remain underexplored (Bastiaanssen et al., 1998; Bonan et al., 2002; Cea et al., 2005; Idso, 1981; Kustas and Norman, 1996; Kustas et al., 2003; Prihodko and Goward, 1997; Quattrochi and Luvall, 2004). This gap is particularly concerning given the unique environmental and geological characteristics of these regions, which can significantly influence thermal dynamics (Anisimov et al., 2010; Anisimov et al., 2007; Assessment, 2005).

Previous studies have primarily focused on the relationship between LST and urban heat islands in non-arid regions, often neglecting the role of lithological formations and their thermal

properties (Jiang and Tian, 2010). For instance, while the impact of urbanization on LST has been well-documented (Chaithanya et al., 2017). For instance, while the impact of urbanization on LST has been well-documented (Ibrahim and Abu-Mallouh, 2018). Additionally, the interplay between LST and SST in coastal arid environments has not been thoroughly investigated despite its potential implications for local climate resilience and marine ecosystems.

Recent advancements in remote sensing and geographic information systems (GIS) have revolutionized our ability to measure and monitor land surface temperature and sea surface temperature with unprecedented accuracy and spatial resolution (Al Kuwari et al., 2016; Jensen et al., 2005; Khandelwal et al., 2018; Kim, 1992; Tarrad and Ibrahim, 2021). (McMillin, 1975). In addition, to avoid many obstacles that can be faced during this process, several studies have presented different approaches to deal with issues such as atmospheric and emissivity effects (Becker and Li, 1990; Gillespie et al., 1998; Hook et al., 1992; Ibrahim and Abu-Mallouh, 2018; Ibrahim et al., 2021; Jiménez-Muñoz and Sobrino, 2003; Kealy and Hook, 1993; Kerr et al., 1992; Vázquez et al., 1997). The current study addresses these gaps by leveraging remote sensing and GIS techniques to estimate LST and SST in Aqaba, Jordan, a rapidly urbanizing coastal city characterized by diverse geological formations. The primary objective is to explore the relationships between temperature variations, land use changes, and lithological features. Specifically, the study aims to quantify the impact of urbanization and geological formations on LST, with a focus on identifying thermal anomalies in urban and exposed geological areas, additionally to investigate the correlation between LST and SST along the Red Sea coast, providing insights into the land-sea thermal interactions in arid coastal environments.

The study hypothesizes that land use and lithology variations significantly influence LST, with urban areas and silica-rich geological formations exhibiting higher temperatures. A measurable correlation exists between LST and SST, driven by the thermal exchange between terrestrial and marine environments. This research contributes to a deeper understanding of thermal dynamics in arid coastal regions by addressing these objectives, offering valuable insights for urban planning, environmental management, and climate change adaptation strategies.

STUDY AREA

Aqaba is located in the southernmost parts of Jordan at 29°00’ to 30°50’ N and 35°00′ to 36°40’ E (Figure 1). It spans an area of 4940 km² The area hosts a wide variation of topographic features where rugged mountains (up to ca. 1848 m

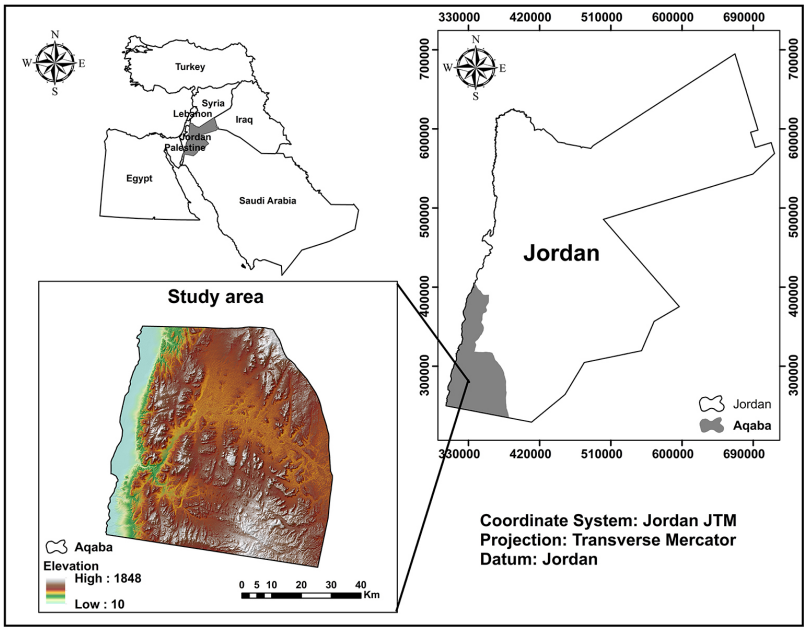

Figure 1. Location map of the Aqaba area; lower-left – digital elevation model of the study area based on DEM

above sea level (asl)) are found in the east and north, while flat areas (ca. 10 m asl) are located in the southern and western parts (Al-Taani et al., 2023; Burdon, 1959). The contemporary climate is arid, with a mean annual rainfall of ca. 32.2 mm (Farhan and Anaba, 2016). The highest summer temperature during July reaches up to about 37°C while it drops to about 23°C at night, with a summer daily average of 11.4 sunny hours (Al-Ghriybah and Didane, 2023).

Geological settings

The study area is primarily comprised of Proterozoic igneous rocks, locally known as the Aqaba Complex, which includes granites and granodiorites in the highlands in the study area's central and western parts. Several sedimentary formations are found either overlying the Aqaba Complex or exposed at different locations. These include the Cambrian Ram sandstone (Salib Arkose) formation consisting of more than 50 m yellowish pebbly conglomerate and arkosic sandstone. The particle size fines upward where sedimentary structures are noted on the Natural Resources Authority (NRA) map. The Cenomanian Kurnub sandstone formation is also exposed over a small area in the northeastern parts of the study area. This formation primarily consists of fine to coarse sandstone with pebbles of quartz (NRA map). Over the eastern parts of the study area, the Cambrian sandstone Khreim formation is exposed (Powell et al., 2014). In addition to the sandstone formations, the limestone-dominated Ajlun and Amman Wadi Sir formations are exposed (Masri, 1963). The western parts of the study area, influenced by the drainage originating from the central highlands, are covered by Quaternary to recent deposits that primarily comprise alluvial fans, siliciclastic gravels, sand, mudflats, and wadi sediments. (Smadi, 1997) (Figure 2).

MATERIALS AND METHODS

Data set

This investigation utilizes satellite imagery acquired in April 2022 from the Landsat 8 OLI/ TIRs (Operational Land Imager) and MODIS; specifically, the examination contains records from Landsat 8 OLI and MODIS for estimating land surface temperature. These are free through Global Visualization (GloVis) and the United States Geological Survey (USGS) website. In addition, daily Level 3 sea surface temperature data from MODIS through the Ocean Color Database of the National Aeronautics and Space Administration (NASA) with a resolution of 4 km. The data were also obtained from in-situ measurements and calibrated to align with in-situ sea surface temperature readings, as shown in Table 1. Furthermore, the geological map produced by the Jordan Natural Resources Authority was utilized to establish the correlation between land surface temperature and the geological formations in the study area. The data was preprocessed through the use of a set of different software, including ERDAS IMAGINE 2014 for image processing, ArcMap Software used for land use and land cover classification, accuracy assessment of applying the LST equation, and R Studio for statistical analysis (Figure 3).

The study employs a combination of remote sensing data and statistical analysis to investigate the correlation between land surface temperatures and sea surface temperature based on the Methodology used. LST was estimated using the split-window algorithm applied to Landsat 8 OLI/ TIRS thermal bands, while SST was derived from MODIS Level 3 data with a spatial resolution of 4 km. The correlation between LST and SST was analyzed using Pearson's correlation coefficient,

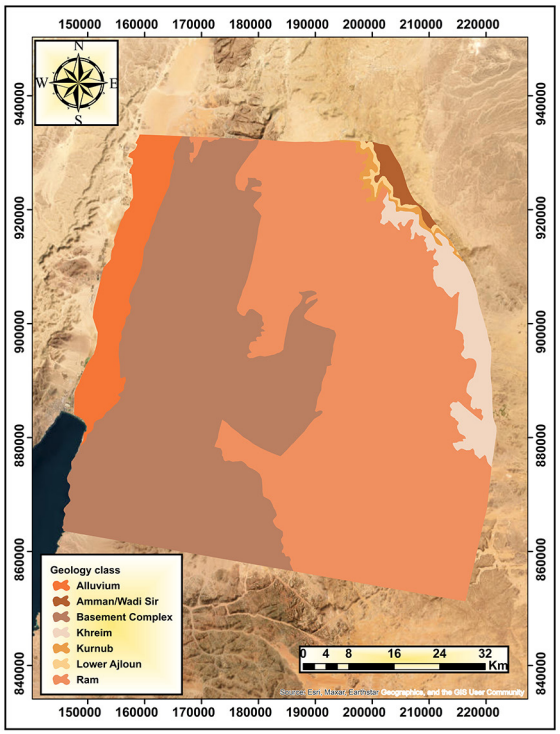

Figure 2. Exposed geological formation map for the study area (after Smadi 1997)

Table 1. Factors used in the study

Data set	Source	Resolution	Factors
Digital elevation model	STRM	30 m	Elevation
Landsat 8	USGS	30 m	LULC, LST
MODIS	NASA	4 km	LST, SST
Lithology	Ministry of energy and mineral resources	1:50000	Lithology map

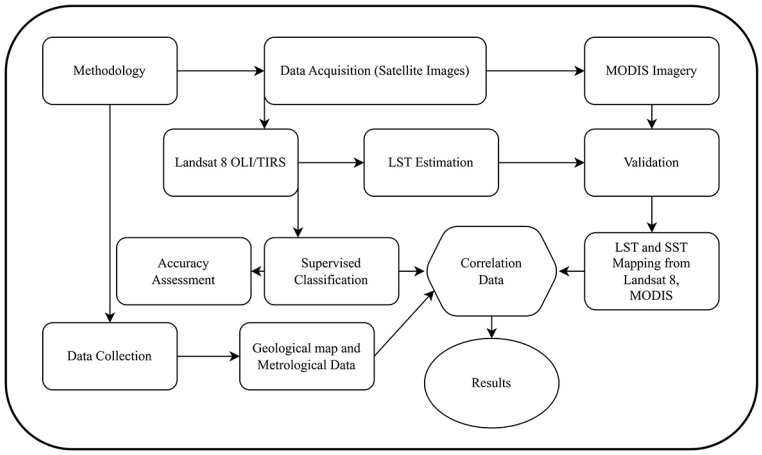

Figure 3. Methodology flow chart for the study

quantifying the linear relationship between the two variables. This approach allows for a robust assessment of the study area's thermal interactions between terrestrial and marine environments.

Image processing

Various methods, such as dual-angle (DA), split-window (SW), and single-channel (SC), are employed for estimating land surface temperature. In the split-window approach, thermal bands and NDVI data are utilized, and the LST can be derived using Equation (1). (Alipour et al., 2003; Ghulam and Hall, 2010; Rajeshwari and Mani, 2014).

$$LST = \frac{BT}{1} + \left(W \times \frac{BT}{P} \times \ln(e)\right) \quad (1)$$

where: the *LST* is land surface temperature, *BT* is brightness temperature and *W* is wavelength, *P* is a constant value of 1438, and *e*/*LSE* refers to the land surface emissivity.

Brightness temperature (BT)

According to NASA (2012) the brightness temperature can be defined as the blackbody temperature that produces the light sensed by the sensor. At the same time, Alipour et al. (2003) define it as the temperature recorded by the satellite when the image is acquired. Hence, it is a satellite-generated temperature and does not reflect on-ground temperatures (Alipour et al., 2003). Accordingly, TIRS band data (as BT) can be obtained by converting thermal constants in the metadata using Equation 2.

$$T = \frac{K2}{ln\left(\frac{K1}{l\lambda} + 1\right)} - 272.15 \quad (2)$$

where: the K1 and K2 are thermal constants, Lλ refers to the top of atmospheric spectral radiance.

The BT is calculated, considering the top of atmospheric (TOA) spectral radiance is acquired, as shown in Equation 3.

$$L\lambda = M_L \times Qcal + A \quad (3)$$

The M_L refers to the Band specific multiplicative rescaling factor (radiance_mult_band_10/11). A_L means the Band specific additive rescaling factor (radiance_add_band_10/11). Qcal is a band 10/ 11 image.

Land surface emissivity

A relative parameter known as land surface emissivity can be used to calculate blackbody radiance from the land surface temperature (Sobrino et al., 2008). There are various methods for

estimating the emissivity of the terrestrial surface (Equation 4). The NDVI approach is used, which calculates the LST in degrees Celsius after accounting for the proportion of vegetation (Pv). Equation 5 is used for land surface emissivity.

$$e = 0.004 \times PV + 0.9 \quad (4)$$

$$Pv = \left(\frac{NDVI - NDVImin}{NDVImax - NDVImin}\right)^2 \quad (5)$$

where: the e refers to LSE (land surface emissivity), the P_v is the proportion of vegetation. NDVI – normalized differences vegetation index.

Image classification

Satellite data was obtained from the USGS Earth Explorer. The maximum likelihood method was employed to classify the land use map, which is considered one of the most common methods used in Supervised classification (Ibrahim and Abu-Mallouh, 2018). Two hundred points were sampled to establish the training samples for each class.

Accuracy assessments

The accuracy assessments provide deeper insights into the areas where classification errors occur. To evaluate the precision of the classification, a set of random points needs to be generated, allowing for the analysis of data at each point's location. This process helps determine the overall accuracy of the categorization. The outcome would be determining, using Google Earth (truth points), the type of land use at that location and contrasting it with the land use of the classified raster (Jensen, 2005). The classification accuracy was evaluated using three common criteria: overall accuracy, producer accuracy, and user accuracy (Lillesand et al., 2015)

It is calculated using Equations (6 and 7)

$$Accuracy = \frac{TP+TN}{TP+TN+FP+FN} \quad (6)$$

$$Precision = \frac{TP}{TP+FP} \quad (7)$$

Sea surface temperature

The MODIS SST was retrieved using the NLSST algorithm given in Equation 8:

$$Ts = \alpha + \beta' Ti + \gamma'(Ti - Tj) + \delta(1 - sec(\theta)) \quad (8)$$

where: the Ti's are brightness temperatures in various bands for a given location and the coefficients α, β and γ give the parameterized correction, θ is the zenith angle and δ is an additional scan angle coefficient (Minnett, 1990; Walton et al., 1998).

RESULTS AND DISCUSSION

Observed and estimated land surface temperature

Land surface temperature were estimated using TIR and MODIS images satellite data. Figure 4 illustrates the geographical distribution of land surface temperature, where the values ranged from 24 °C to 50 °C (mean = 37 °C). Elevated (high) surface temperatures are shown as dark red, covering the northeastern and central regions of the study area.

Similarly, Figure 5 shows the observed surface temperature (MODIS image). In agreement with the LST distribution, the dark red color (high) values are concentrated in the northeastern and central parts with values ranging from 33 °C to 50 °C (mean = 42 °C). This was also emphasized through statistical correlation between the two maps, where an r2 value of 0.64 was obtained

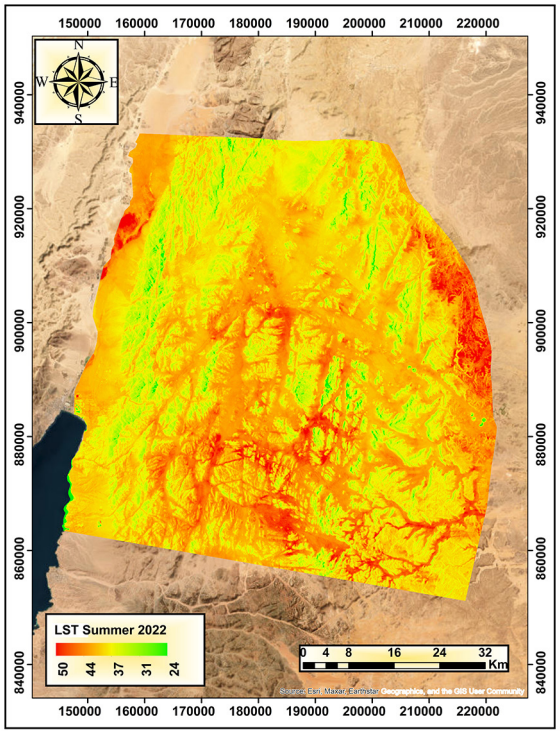

Figure 4. Estimated land surface temperature map

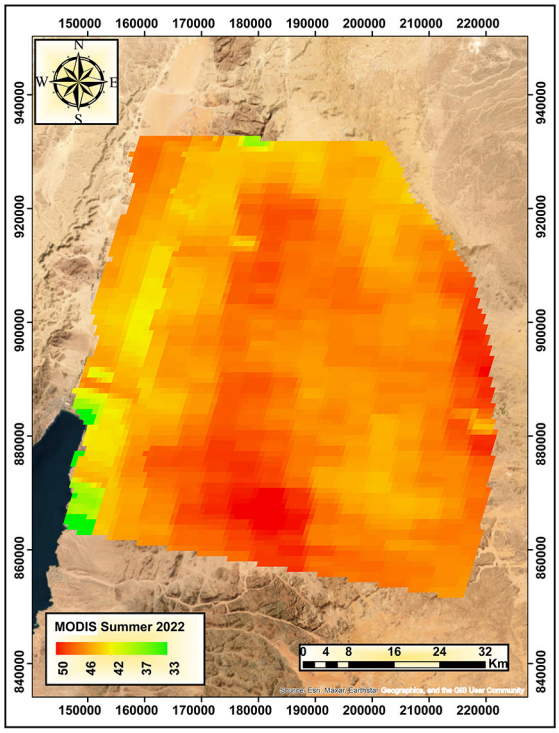

Figure 5. Observation surface temperature (MODIS image)

(for 200 control points). However, minor differences between the two maps are noticeable, likely due to variations in spatial resolution among the data sources and the influence of surface roughness on temperature measurements (Lillesand et al., 2015), as well as the potential influence of atmospheric impurities on surface temperature.

LST and land use changes

Image classification divided The study area into four land use types (Figure 6). These include exposed geological formations (barren), vegetation, urban areas, and water. When analyzing the reference data and the classified results in Table 2, it was observed that 77.35% of the exposed geological formations were correctly classified. (user accuracy percentage) with a moderate level of agreement, as suggested by a Kappa coefficient of 0.73. and an overall accuracy of 79% was obtained from reference data and the classification output. By extracting data for 25 points, the LST and MODIS-temperature data were compared for accuracy and consistency, as shown in Table 2. Figure 7 shows that the two methods consistently classified vegetation cover regardless of the higher temperatures observed using the MODIS data. Regarding the urban and barren classes, the results indicate some discrepancies between the two methods. The urban class was better classified using the LST data, while the barren class showed more consistent classification using the MODIS data; the spectral signature of metropolitan areas is very similar to that of neighboring areas due to the common materials, such as limestone, present in both. This similarity poses challenges for accurately classifying urban areas in rocky and arid regions using satellite imagery, which often lacks high resolution. This issue is consistent with the problems highlighted by (Tarrad and Ibrahim, 2021) regarding the classification difficulties in such environments. The findings reveal a reasonable correlation between the observed surface temperature and the LST derived from the single-channel algorithm using Landsat OLI/TIRS sensor data, as reflected in the minimum, maximum, mean, and standard deviation values. The results also reveal that the accuracy of these data is low when compared to points for each class between LST data and MODIS data, except for the barren areas class, which exhibits good accuracy.

Lithological formations and estimated temperature

Seven lithological formations, namely the basement complex, alluvium, Lower Ajloun,

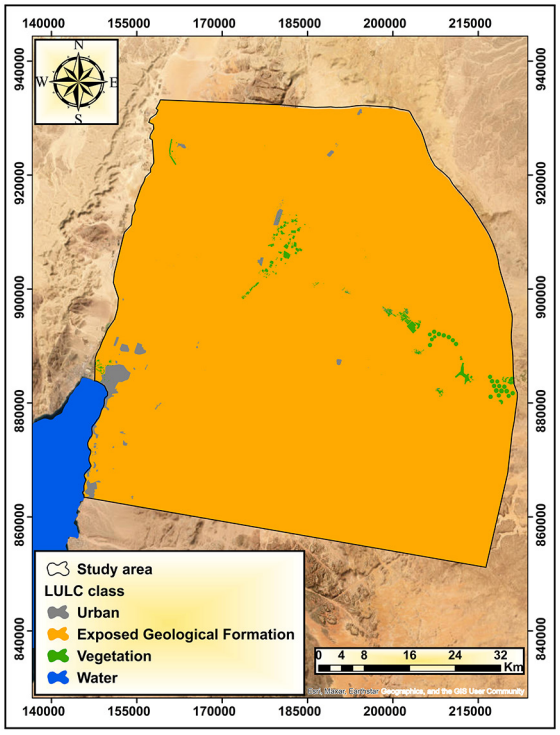

Figure 6. Land use map for the study area

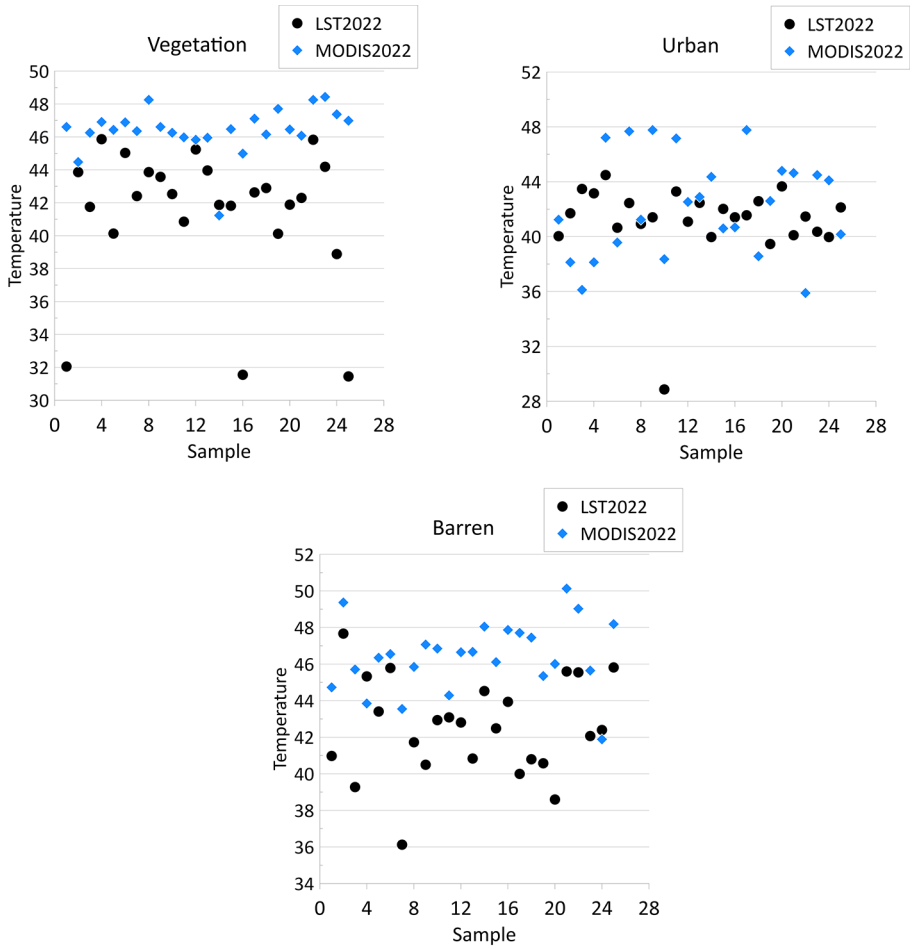

Figure 7. Temperature data for the 25 points extracted from the different land use classes

Amman-Wadi Sir, Kornub, Khreim, and Ram, are exposed in the study area (see section 2.1). By superposing the lithological map over the measured LST map (Figure 8), the results indicate that the lithological variations are also observed in terms of temperature variability. The highest surface temperature was observed in the basement complex and alluvium deposits, while other formations showed lower average temperatures. This can be attributed to the mineralogical content of the different rocks where higher temperatures reflect the silica in igneous rocks; similarly, the silica content in the sandstone formations may have also contributed to the elevated temperatures obtained. (Ibrahim and Abu-Mallouh, 2018; Ibrahim et al., 2021; Tarrad and Ibrahim, 2021) confirmed in their studies that there is a correlation between basalt and LST using satellite images. Other formations, such as limestone-dominated formations, may exhibit a weak correlation between their mineral composition and energy, which can cause energy reflection or water retention, ultimately reducing land temperature.

To better understand the lithological discrimination using the measured temperatures, 25 points were selected and numerically examined. The results also revealed that the data is more dispersed when looking at the LST data, compared to the MODIS data, except for the basement complex and alluvium formation, which exhibit good similarity between LST and MODIS data. Additionally, to show the difference in data consistency between the two methods, the 25 points were plotted in Figure 9. Similarly to the statistical parameters, the visual inspections show that the MODIS temperature data is more consistent than the LST data. Nonetheless, the MODIS data shows higher temperatures for the lithological formations.

It has been noted that surface temperatures exhibit elevated values across various land use types and geological formations. It is worth noting that vegetation and urban areas have experienced slightly lower values in average temperatures. This could be attributed to factors such as water-cooling in vegetation or the presence of vegetation cover, which has a weak correlation

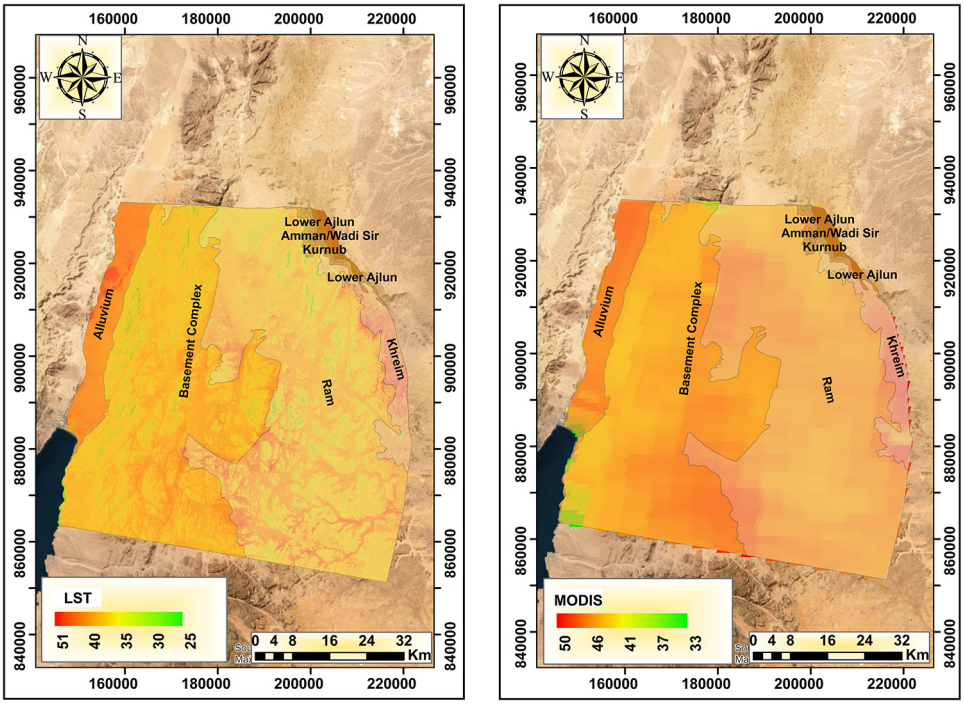

Figure 8. A lithological map of the study area overlies the LST map (a) and MODIS map (b)

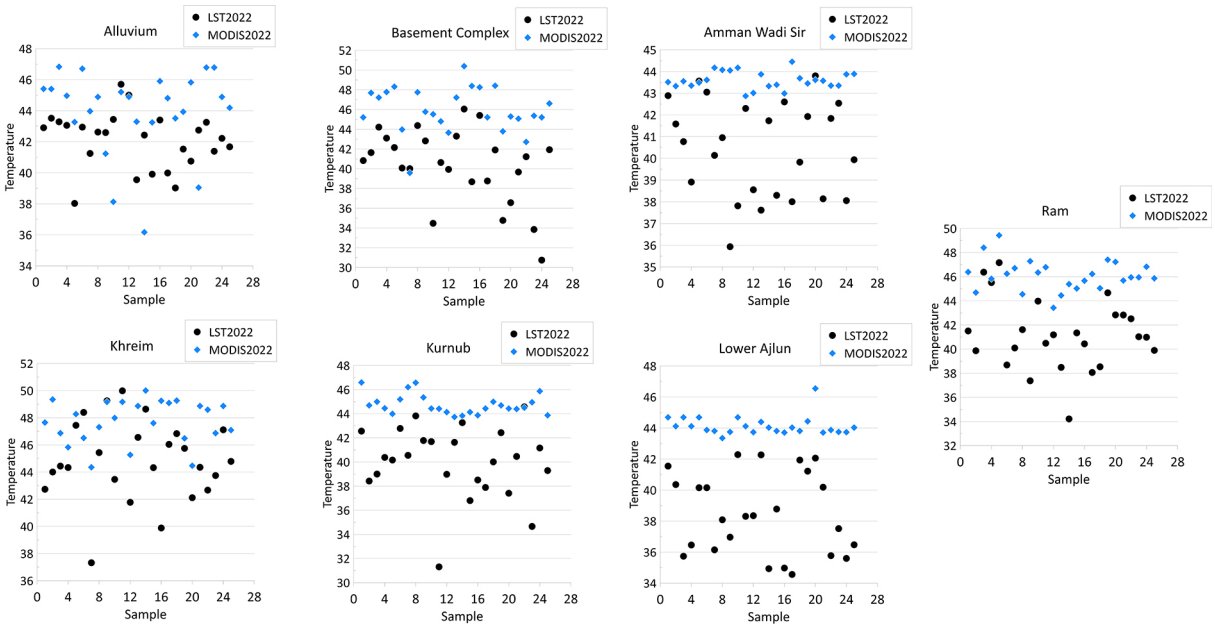

Figure 9. Temperature data for the 25 points extracted from the different lithological formations

with surface temperature. Increasing vegetation cover can lead to a decrease in surface temperature. Additionally, Utilizing reflective building materials or cooling systems in urban areas during the summer can help lower temperatures. This is particularly beneficial in arid and semi-arid regions, where high temperatures persist most of the year. The highest values in surface temperature of the urban areas were observed for built-up land constructed over the alluvium and basement complex formations. In contrast, other urban areas in other formations showed lower average temperatures. This can be attributed to the effect of these geological formations on residential areas, which result in higher temperatures than other areas.

Relationship between SST, LST, and land use changes

As discussed in advance, we will look at discovered distinct spatial styles in land surface temperature and sea surface temperature, especially along the coast of the Red Sea. The calculated LST exhibited lower values near the ocean coast, indicating a capacity correlation with SST variations. Figure 10 illustrates that SST ranged from 26.5°C to 28.Five°C, with a mean of 27.5°C. Higher SSTs were predominantly located in the southern parts of the Red Sea, suggesting complicated environmental effects on temperature distribution.

The correlation between LST and SST underscores the interconnectedness among terrestrial and marine thermal dynamics. In all likelihood, Coastal geomorphology, including bays, estuaries, and headlands, modulates oceanic circulate patterns and heat change approaches, thereby affecting SST variability. Furthermore, land use changes, mainly urbanization and exposed geological formations, affected neighborhood temperature gradients noticeably. Urban heat islands and thermal anomalies in exposed geological formations contribute extra warmth to adjoining coastal waters, doubly raising SST. This mutualistic relationship between land and sea temperatures can lead to comments mechanisms affecting local weather dynamics.

Understanding those interactions is essential for assessing coastal regions' weather resilience and environmental sustainability. By elucidating the reciprocal influences of LST and SST, this study contributes valuable insights into how anthropogenic activities and natural strategies form temperature regimes at the land-water interface. These findings tell strategies for mitigating urban warmth influences and spotlight the significance of integrated land-sea control techniques in mitigating weather alternate results.

Generally, The analysis revealed a significant correlation (r = 0.75) between LST and SST, particularly in coastal areas. This correlation underscores the interconnectedness between terrestrial and marine thermal dynamics, where higher LST values in urban and exposed geological areas contribute to elevated SST in adjacent coastal waters. The statistical significance of this relationship was confirmed using a p-value threshold of 0.05, indicating that the observed correlation is not due to random chance. These findings highlight the influence of land-based thermal anomalies on coastal marine environments, providing valuable insights for understanding the land-sea thermal interactions in arid coastal regions.

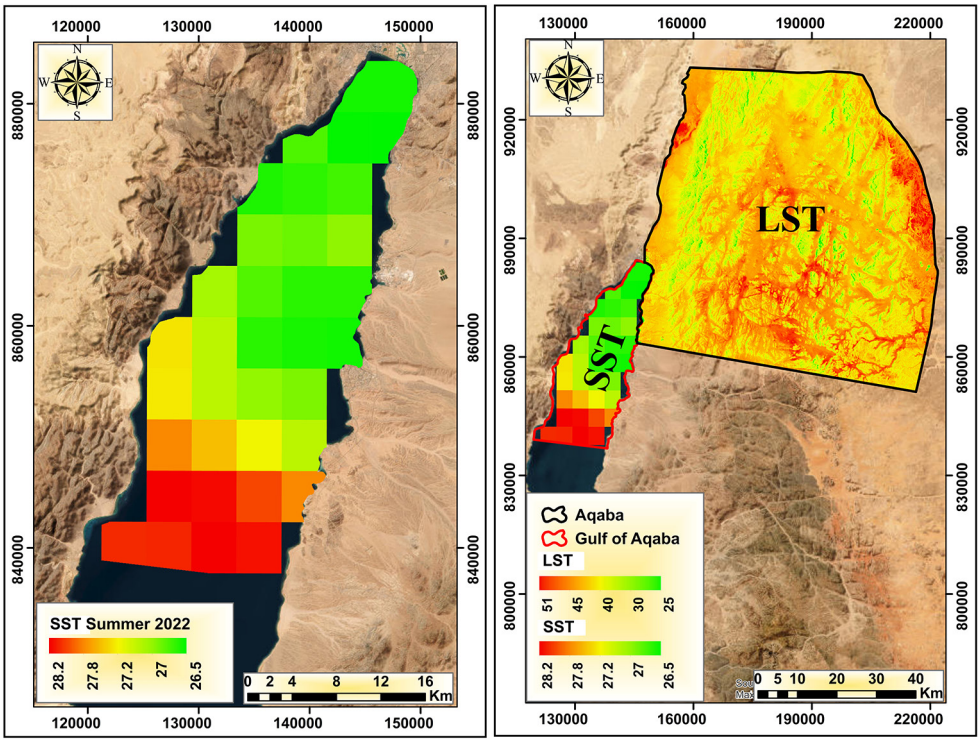

Figure 10. Observation of sea surface temperature (MODIS image) (a) and a combined map showing the LST values relative to SST values (b)

LIMITATIONS AND FUTURE DIRECTIONS

It is critical to notice several obstacles in estimating land surface temperature using far-off sensing strategies in Aqaba, Jordan. Challenges include uncertainties due to cloud cowl and atmospheric conditions, affecting LST accuracy, especially in dynamic coastal and urban environments. The spatial resolution of Landsat eight OLI and MODIS data limits the detection of first-rate-scale temperature versions inside heterogeneous landscapes, suggesting the want for better-decision imagery or UAV integration. Future studies must additionally explore the complexities of urban heat islands, integrating socio-economic elements to enhance knowledge. Additionally, validating fashions like the split-window algorithm (SWA) with floor-based measurements should improve reliability and applicability in environmental tracking and urban planning contexts.

CONCLUSIONS

Different mathematical methods are discussed in the literature to estimate LSTs using BT of thermal bands extracted from TIRS sensors and LSE derived from the PV extracted from OLI sensors. From these methods, the split-window algorithm has proven to be efficient and report sensible data. In this study, supervised classification of the obtained satellite images is used to generate the land use map of the study area, resulting in four distinct land use classes with an overall accuracy of 79%: rock, vegetation, urban areas, and water.

Analysis of the LST images revealed higher surface temperatures in areas covered by igneous and silica-rich sedimentary formations. Additionally, the results indicate a moderate relationship between land surface temperature and the Moderate Resolution Imaging Spectroradiometer (MODIS). Therefore, the SW algorithm can be utilized to compute land surface temperature by employing Landsat 8 multiband operational land imager and thermal infrared sensor images. Moreover, this algorithm can detect differences in land temperature among various geological formations, indicating that the estimated land surface temperature is a valuable tool for lithological mapping and monitoring hydrothermal dynamics, provided that reliable data and techniques are available. The results also indicate higher temperatures in residential areas near igneous and silica-rich formations.

In addition to the findings discussed, this study highlights several implications for future research. Firstly, it is crucial to expand the scope of research to consist of lengthy-term monitoring and predictive modeling of city heat islands and their influences on neighborhood climate resilience. By incorporating ancient satellite data statistics and in-situ measurements, future studies can elucidate temporal traits in LST and SST, facilitating proactive measures to mitigate environmental risks and enhance community resilience against climate variability. Moreover, future research could integrate multi-sensor data, including MODIS, to comprehensively monitor thermal dynamics at varying spatial and temporal scales. This approach would provide a more nuanced understanding of how land use changes and geological attributes influence surface temperatures over time. Exploring these relationships can contribute to improved land management strategies, climate change adaptation efforts, and sustainable urban planning practices in rapidly developing coastal regions like Aqaba.

Acknowledgment

The authors are immensely grateful to the Supreme Council of Science and Technology in Jordan for supporting this research, to the Al al-Bayt University for providing geological data, to reviewers in the Journal of Ecological Engineering and Environmental Technology, and to the USGS/Landsat for giving the free data.

REFERENCES

1. Al-Ghriybah, M., & Didane, D. H. (2023). Development of wind-solar maps in aqaba, jordan as potential sources for power generation. *Journal of Applied Engineering Science*, *21*(1), 212–223.
2. Al-Taani, A., Al-husban, Y., & Ayan, A. (2023). Assessment of potential flash flood hazards. Concerning land use/land cover in Aqaba Governorate, Jordan, using a multi-criteria technique. *The Egyptian Journal of Remote Sensing and Space Science*, *26*(1), 17–24.
3. Al Kuwari, N., Ahmed, S., & Kaiser, M. (2016). Optimal satellite sensor selection utilized to monitor the impact of urban sprawl on the thermal environment in doha city, Qatar.

4. Alipour, T., Sarajian, M., & Esmaeily, A. (2003). Land surface temperature estimation from thermal band of landsat sensor, case study: Alashtar city. *The International Achieves of the Photogrammetry, Remote Sensing and Spatial Information Sciences*, *38*(4), 1–6.
5. Anisimov, O., Belolutskaya, M., Grigoriev, M., Instanes, A., Kokorev, V., Oberman, N., Reneva, S., Strelchenko, Y., Streletskiy, D., & Shiklomanov, N. I. (2010). Major natural and social-economic consequences of climate change in the permafrost region: predictions based on observations and modeling. *Moscow: Greenpeace*.
6. Anisimov, O. A., Vaughan, D. G., Callaghan, T. V., Furgal, C., Marchant, H., Prowse, T. D., Vilhjálmsson, H., & Walsh, J. E. (2007). Polar regions (arctic and antarctic). *Climate change*, *15*, 653–685.
7. Assessment, A. C. I. (2005). Arctic Climate Impact Assessment (ACIA) scientific report.
8. Bastiaanssen, W. G., Menenti, M., Feddes, R., & Holtslag, A. (1998). A remote sensing surface energy balance algorithm for land (SEBAL). 1. Formulation. *Journal of hydrology*, *212*, 198–212.
9. Becker, F., & Li, Z.-L. (1990). Towards a local split window method over land surfaces. *Remote Sensing*, *11*(3), 369–393.
10. Bonan, G. B., Oleson, K. W., Vertenstein, M., Levis, S., Zeng, X., Dai, Y., Dickinson, R. E., & Yang, Z.-L. (2002). The land surface climatology of the Community Land Model coupled to the NCAR Community Climate Model. *Journal of Climate*, *15*(22), 3123–3149.
11. Burdon, D. J. (1959). Handbook of the geology of Jordan: to accompany and explain the 3 sheets of the 1: 250,000 geological map of Jordan East of the Rift by Albert M. Quennell.
12. Cea, C., Cristóbal, J., Serra, P., & Pons, X. (2005). Mejoras en la detección semiautomática de nubes y sombras en imágenes Landsat. XI Congreso Nacional de Teledetección, Puerto de la Cruz. Tenerife,
13. Chaithanya, V., Binoy, B., & Vinod, T. (2017). Estimation of the Relationship between urban vegetation and land surface temperature of Calicut City and suburbs, kerala, India using GIS and Remote Sensing data. *International Journal of Advanced Remote Sensing and GIS*, *6*(1), 2088–2096.
14. Farhan, Y., & Anaba, O. (2016). Flash flood risk estimation of Wadi Yutum (Southern Jordan) watershed using GIS based morphometric analysis and remote sensing techniques. *Open Journal of Modern Hydrology*, *6*(2), 79.
15. Ghulam, A., & Hall, M. (2010). Calculating surface temperature using Landsat thermal imagery. *Online: https://serc. carleton. edu/files/NAGTWorkshops/gis/activities2/student_handout_calculating_te. pdf (accessed 25 March 2016). Ghulam A*.
16. Gillespie, A., Rokugawa, S., Matsunaga, T., Cothern, J. S., Hook, S., & Kahle, A. B. (1998). A temperature and emissivity separation algorithm for Advanced Spaceborne Thermal Emission and Reflection Radiometer (ASTER) images. *IEEE transactions on geoscience and remote sensing*, *36*(4), 1113–1126.
17. Hook, S. J., Gabell, A. R., Green, A. A., & Kealy, P. S. (1992). A comparison of techniques for extracting emissivity information from thermal infrared data for geologic studies. *Remote Sensing of Environment*, *42*(2), 123–135.
18. Houghton, R. A., & Woodwell, G. M. (1989). Global climatic change. *Scientific American*, *260*(4), 36-47.
19. Ibrahim, M., & Abu-Mallouh, H. (2018). Estimate land surface temperature in relation to land use types and geological formations using spectral remote sensing data in Northeast Jordan. *Open Journal of Geology*, *8*(2), 174–185.
20. Ibrahim, M., Koch, B., & Datta, P. (2021). Evaluate the effect of land surface temperature in arid and semi-arid lands using potential remote sensing data and GIS techniques. *International Journal of Global Warming*, *24*(3–4), 342–355.
21. Idso, S. B. (1981). A set of equations for full spectrum and 8-to 14-μm and 10.5-to 12.5-μm thermal radiation from cloudless skies. *Water Resources Research*, *17*(2), 295–304.
22. Jensen, J. R. (2005). Digital image processing: a remote sensing perspective. *Upper Saddle River, NJ: sPrentice Hall*.
23. Jensen, R. R., Gatrell, J. D., McLean, D. D., Weng, Q., & Larson, R. C. (2005). Satellite remote sensing of urban heat islands: current practice and prospects. *Geospatial technologies in urban environments*, 91–111.
24. Jiang, J., & Tian, G. (2010). Analysis of the impact of land use/land cover change on land surface temperature with remote sensing. *Procedia Environmental Sciences*, *2*, 571–575.
25. Jiménez-Muñoz, J. C., & Sobrino, J. A. (2003). A generalized single-channel method for retrieving land surface temperature from remote sensing data. *Journal of geophysical research: atmospheres*, *108*(D22).
26. Kealy, P. S., & Hook, S. J. (1993). Separating temperature and emissivity in thermal infrared multispectral scanner data: Implications for recovering land surface temperatures. *IEEE transactions on geoscience and remote sensing*, *31*(6), 1155–1164.
27. Kerr, Y. H., Lagouarde, J. P., & Imbernon, J. (1992). Accurate land surface temperature retrieval from AVHRR data with use of an improved split window algorithm. *Remote Sensing of Environment*, *41*(2–3), 197–209.
28. Khandelwal, S., Goyal, R., Kaul, N., & Mathew, A. (2018). Assessment of land surface temperature

variation due to change in elevation of area surrounding Jaipur, India. *The Egyptian Journal of Remote Sensing and Space Science*, *21*(1), 87–94.

29. Kim, H. H. (1992). Urban heat island. *International Journal of Remote Sensing*, *13*(12), 2319–2336.
30. Kustas, W., & Norman, J. (1996). Use of remote sensing for evapotranspiration monitoring over land surfaces. *Hydrological Sciences Journal*, *41*(4), 495–516.
31. Kustas, W. P., French, A. N., Hatfield, J. L., Jackson, T. J., Moran, M. S., Rango, A., Ritchie, J. C., & Schmugge, T. J. (2003). Remote sensing research in hydrometeorology. *Photogrammetric Engineering & Remote Sensing*, *69*(6), 631–646.
32. Lillesand, T., Kiefer, R. W., & Chipman, J. (2015). *Remote sensing and image interpretation*. John Wiley & Sons.
33. Masri, M. (1963). *Report on the geology of the Amman Zarqa area*. C. w. Authority.
34. McMillin, L. M. (1975). Estimation of sea surface temperatures from two infrared window measurements with different absorption. *Journal of Geophysical Research*, *80*(36), 5113–5117.
35. Merigan, W. H., & Weiss, B. (1980). *Neurotoxicity of the visual system* (Vol. 11). Raven Press.
36. Minnett, P. (1990). The regional optimization of infrared measurements of sea surface temperature from space. *Journal of Geophysical Research: Oceans*, *95*(C8), 13497–13510.
37. NASA. (2012). National Aeronautics and Space Administration. Goddard Earth Sciences (GES) Data and Information Services Center (DISC). https://daac.gsfc.nasa.gov/
38. Powell, J. H., Abed, A. M., & Le Nindre, Y.-M. (2014). Cambrian stratigraphy of Jordan. *GeoArabia*, *19*(3), 81–134.
39. Prihodko, L., & Goward, S. N. (1997). Estimation of air temperature from remotely sensed surface observations. *Remote sensing of environment*, *60*(3), 335–346.
40. Quattrochi, D. A., & Luvall, J. C. (2004). *Thermal remote sensing in land surface processing*. CRC Press.
41. Rajeshwari, A., & Mani, N. (2014). Estimation of land surface temperature of Dindigul district using Landsat 8 data. *International journal of research in engineering and technology*, *3*(5), 122–126.
42. Santer, B. D., Taylor, K. E., Wigley, T. M., Johns, T., Jones, P., Karoly, D., Mitchell, J., Oort, A., Penner, J., & Ramaswamy, V. (1996). A search for human influences on the thermal structure of the atmosphere. *Nature*, *382*(6586), 39–46.
43. Smadi, A. A. (1997). *National Geological Mapping Project Report*. N. R. a. (NRA).
44. Sobrino, J. A., Jiménez-Muñoz, J. C., Sòria, G., Romaguera, M., Guanter, L., Moreno, J., Plaza, A., & Martínez, P. (2008). Land surface emissivity retrieval from different VNIR and TIR sensors. *IEEE transactions on geoscience and remote sensing*, *46*(2), 316–327.
45. Stanhill, G., & Cohen, S. (2001). Global dimming: a review of the evidence for a widespread and significant reduction in global radiation with discussion of its probable causes and possible agricultural consequences. *Agricultural and forest meteorology*, *107*(4), 255–278.
46. Tarrad, M., & Ibrahim, M. (2021). Detection of Limestone Quarries in Jordan Through Remote Sensing Data to Achieve Sustainable Utilization in Vernacular Architecture. *International Journal of Sustainable Development & Planning*, *16*(4).
47. Vale, M. M., Berenguer, E., de Menezes, M. A., de Castro, E. B. V., de Siqueira, L. P., & Rita de Cássia, Q. P. (2021). The COVID-19 pandemic as an opportunity to weaken environmental protection in Brazil. *Biological Conservation*, *255*, 108994.
48. Vázquez, D. P., Reyes, F. O., & Arboledas, L. A. (1997). A comparative study of algorithms for estimating land surface temperature from AVHRR data. *Remote Sensing of Environment*, *62*(3), 215–222.
49. Walton, C., Pichel, W., Sapper, J., & May, D. (1998). The development and operational application of nonlinear algorithms for the measurement of sea surface temperatures with the NOAA polar-orbiting environmental satellites. *Journal of Geophysical Research: Oceans*, *103*(C12), 27999–28012.
50. Warrick, R., Azizul Hoq Bhuiya, A., & Mirza, M. (1996). *The greenhouse effect and climate change*. Springer.
51. Wigley, T. M., & Raper, S. C. (1990). Natural variability of the climate system and detection of the greenhouse effect. *Nature*, *344*(6264), 324–327.